Discrete Anisotropy Model of Heterogeneous Cardiac Tissue Predicting the Occurrence of Symmetry Breaking of Reentrant Activity

S. A. Romanova [+*], A. K. Berezhnoy [+*×], L. E. Ruppel [+], A. A. Aitova [+*], S. S. Bakumenko [+×],
I. S. Semidetnov [+], V. D. Naumov [+], M. M. Slotvitsky [+*×], V. A. Tsvelaya [+*×1)], K. I. Agladze [+*1)]

[+] *Laboratory of Experimental and Cellular Medicine, Moscow Institute of Physics and Technology, 141701 Dolgoprudny, Russia*

[*] *M. F. Vladimirsky Moscow Regional Research Clinical Institute, 129110 Moscow, Russia*

[×] *ITMO University, 197101 St. Petersburg, Russia*

Cardiac arrhythmias are a major cause of cardiovascular mortality worldwide. Functional heterogeneity of cardiac tissue is an inevitable arrhythmogenic condition that may create nonlinear wave turbulence or reentry with subsequent arrhythmia initiation. The relation between propagation heterogeneity and the onset of reentry is of great theoretical and practical importance. Here, we present a conceptual representation of heterogeneous tissue expressed through alternating local and global tissue anisotropy with discreteness of membrane conductance. To contrast the influence of distributed heterogeneity, we investigated the interaction of a high-frequency wavetrain at a sharp anisotropy-symmetric obstacle. The revealed tendency of a heterogeneous system to form reentry was formalized into the single concept of a vulnerable frequency corridor that can be estimated experimentally. Using the joint *in vitro–in silico* approach, we defined an anomalous stable growth of a unidirectional block in the vicinity of an obstacle, depending on the direction of the anisotropy vector. This effect explains the limited applicability of homogeneous models to predicting the occurrence of primary reentry. Furthermore, computer simulations showed the special role played by other possible mechanisms of excitation, as ephaptic intercellular coupling, in the formation of a unidirectional block of conduction and reentry onset, which could not be predicted by conduction velocity measurements.

Introduction. Threshold excitation followed by a refractory state is a key characteristic of excitable media. The alternation of resting, excited and refractory states of a system underlie the spatio-temporal consistency in the reaction–diffusion (Belousov–Zhabotinsky) systems [1, 2], tissue morphogenesis [3, 4], and neurological diseases [5]. In particular, electrical waves synchronize cardiac contraction [6]; consequently, abnormal propagation in cardiac tissue may provide chaotic electrical activity, which desynchronizes the whole heart. The heart fails to self-restore its normal electrical activity once disturbed, like it is for sustained arrhythmias [7]. Therefore, both the coordinated work of the heart and the irreversible transition to dynamic chaos during arrhythmias are based on the spatio-temporal alternation of excited and refractory states.

Cardiac tissue is highly heterogeneous in terms of excitation conduction. Generally, the most important consequence of conduction inhomogeneities is the development of functional blocks followed by formation of reentrant sources of arrhythmias (i.e., spiral waves). The characteristic wavelength and size of the spiral wave core are derivatives of excitability, refractory period (RP) and conduction velocity (CV), thereby significantly exceeding the characteristic size of subcellular heterogeneities, such as gap junction coupling (GJC) [8] and ephaptic intercellular coupling (EpC) between excitable cells [9, 10]. For this reason, breakup of spiral waves is often simulated using homogeneous models [11–13], or if randomly disturbed heterogeneities appear on scales much smaller than the wave front width [14, 15].

However, the primary mechanism of spiral wave formation is still not fully understood [16, 17]. In most cases, unidirectional blocks result from source-sink mismatch [18], when the local current generated by the wave front cannot sufficiently excite the abrupt expansion of tissue in front of it. In this approximation, the behavior of the excitation wave largely depends on the critical radius of the wavefront curvature rather than on wavelength [19]. Experiments showed that in the case

---

[1)]e-mail: valeriyatsvelaya@gmail.com; agladze@yahoo.com

of non-inhibited excitability, wavefront curvature may affect propagation on scales smaller than the cell size, thereby limiting the applicability of classical continuous medium approach in cardiac tissue [20], leastwise in two-dimensional geometry [20, 21]. Hence, oversimplification of subcellular heterogeneities may not be applicable when studying the local sources of reentry in cardiac tissue.

In contrast to randomly [22, 23] and pseudo-randomly [24] distributed cellular heterogeneities, we applied a virtual cardiac monolayer framework [25] based on the Cellular Potts Models (CPMs) [26–28] and then tailored to reproduce the texture of human atrial tissue [29]. The Hamiltonian approach to sorting coefficients in the diffusion (i.e., conductivity) tensor represents a realistic precomputed spatial distribution of $D_{in} > D_{gap} > D_{bound} > 0$ values for the inner membrane conductance, GJC and EpC, respectively. Here, we showed that pre-calculated diffusion tensor made it possible to formulate the global anisotropy of excitation conduction as an alternation of multidirectional anisotropic domains at a cellular level; we also performed morphological examination of cultured cardiomyocytes to reveal self-organization of cells into similar anisotropic domains through cytoskeletal alignment.

We investigated the conditions under which reentrant spiral waves can be generated by a high-frequency planar wavetrain in the vicinity of a rectangular geometrical obstacle [30]. The key idea is that the combination of a rectangular non-conducting obstacle with a global anisotropy direction aligned with one of its sides makes it possible to maintain the symmetry of the obstacle's tip both when anisotropy direction (AD) or anisotropy ratio (AR) are changed (where AR is the ratio of CV along AD and across, AR > 1). This determines the limits within which we can vary conduction inhomogeneities without changing the geometrical trigger of unidirectional block formation, thereby independently studying the influence of apportioned inhomogeneities on the reentry onset.

We formalized the influence on tissue arrhythmogenicity through a relative change in the vulnerable frequency corridor: a set of values of the stimulation period T_{crit} at which reentry formation is possible. Using the joint *in vitro–in silico* approach, we defined that the set of T_{crit} shifts and expands when AD is rotated, while the spiral wave circulation period T_{spiral} and the maximum captured rate (MCR) as derivatives of the RP remain unchanged. We have further studied in silico the dependence of arrhythmogenicity on the mechanism of cellular coupling: we found that D_{bound} type of conduc-

tance directly controls the spread of T_{crit}. Intriguingly, the concomitant changes in longitudinal CV and planar wavefront behavior predicted by the model seem to be resistant to experimental detection.

We illustrate that appropriate transformations in intercellular coupling can preserve the symmetry of RP and CV, but at the same time significantly affect the key parameter T_{crit}, which describes the probability of nonlinear proarrhythmogenic events. This phenomenon of symmetry breaking extends the chain of reasoning about the limits of applicability of the classical homogeneous models, which began with experimental studies [20]. Our simulations showed that EpC appears to play an important role in stabilizing the planar wavefront in the vicinity of non-conducting areas at pre-critical stimulation frequencies. We also discuss how proposed expansion of theoretical concepts makes EpC inhibition a potential mechanism for producing proarrhythmogenic effects bypassing modulation of ionic channels [31]. Therefore, our model can be an efficient tool for studying the relation between propagation heterogeneity and the onset of reentry in morphologically detailed cardiac tissue.

We performed simulations using a mathematical model that was previously developed for procedural generation of atrial tissue in the CPM formalism [29]. Disposition of cell boundaries and junctions reached equilibrium in 50.000 Monte Carlo steps (MCSs). The fixed coordinates were then converted into conductivity values D_{in}, D_{gap}, and D_{bound} linking neighboring pixels (raw code is openly available in GitHub at https://github.com/Tsvelaya/pyVCT-2). Additional input data for the CPM model were consisted of AD fixed strictly in the vertical direction and rectangular obstacle n with its boundary ∂n. Obstacle n was displaced in the lower left quadrant of the sample (cell density inside n was set to zero). In this study, we extended the model with a branched energy term responsible for non-conducting boundary formation with preserved Bayesian optimization parameters from [29], Eq. (1):

$$H = H_{adhesive} + H_{elastic} + H_{protr} +$$
$$+ H_{nuclei} + H_{junctions} + H_{wall} \qquad (1)$$

$$x_s \to x_t : dH_{wall} = \begin{cases} A & \text{if} \quad \rho(x_t, \partial n) < NVX/B \\ 0 & \text{if} \quad \rho(x_t, \partial n) \geq NVX/B \end{cases},$$

where $H_{adhesive}$ describes interactions of cells with the substrate; $H_{elastic}$ describes the elastic properties of the membrane and preservation of the targeted cell volume; H_{protr} is the term describing the protrusion dynamics of the cardiac cells with a limited number of focals; H_{nuclei}

corresponds to higher rigidity of the nuclei compared to the cell body; $H_{\text{junctions}}$ describes the stability of junctions and alignment of the cytoskeletons of the neighboring cells; and a term H_{wall} describes the energy penalty when a cell tries to cross the n boundary ∂n.

In Equation (1), NVX (NVY) is the fixed number of voxels along the X axis (Y axis); $A = 100$ and $B = 40$ are energy and spatial constants, respectively. The A and B values were selected so that the cell deformation at the boundary was approximately equal to half the cell size. The total value of $dH > 0$ at each MCS determines the probability of transition from initial voxel xs to neighboring voxel xt with probability $\sim \exp(-dH)$ (transition with $dH \leq 0$ occurs with probability 1).

Nonlinear waves of electrical excitation were modeled via the Rush–Larsen integration [32, 33] of a reaction-diffusion equation for the transmembrane potential V, Eq. (2):

$$C_m \frac{\partial V}{\partial t} = -(I_{\text{ion}} + I_{\text{stim}}(i, j, t)) +$$

$$+ D_x(i, j) \frac{\partial^2 V}{\partial^2 x} + D_y(i, j) \frac{\partial^2 V}{\partial^2 y}, \qquad (2)$$

where I_{ion} is the total transmembrane ionic current (pA) from the Courtemanche atrial model [34]; C_m is the specific capacitance of a single membrane element (pF); V is the transmembrane potential (mV); and D_x and D_y encode sequences of D_{in}, D_{gap} and D_{bound} values between neighboring pixels vertically and horizontally, respectively. The stimulation current I_{stim} was expressed as a rectangular step $(2\,\text{ms}, 2\,\text{nA})$ with a spatial width of $150\,\mu\text{m}$ along the sample edge. The system was stimulated from the steady state by the first two stimuli with an interval of $350\,\text{ms}$; all subsequent stimuli followed at a variable frequency T. Calculations were performed with a space step of $2.5\,\mu\text{m}$ for both Eq. (1) and Eq. (2) and time step of $0.001\,\text{ms}$ for Eq. (2).

Confluent cell culture monolayers of neonatal rat ventricular cardiomyocytes (NRVM) on aligned polymer nanofibers were used as an experimental model of anisotropic cardiac tissue. The employed protocols for cell isolation [35], alignment of nanofibers on adhesive culture glasses and immunostaining protocols [36] had been described previously. Cardiac cells were isolated from the ventricles of rat pups (Rattus norvegicus, Sprague Dawley breed) of different age (1–4 days). Isolated cells were seeded on the specimens covered with fibronectin (0.16 mg/ml, Gibco, USA, 33016015) in DMEM culture medium (Gibco, USA, 11960) supplemented with 5 % of FBS (Gibco, USA, 10100147) at a concentration 2×10^5 cells/cm^2. After 3–5 days of cultivation, the samples were used for optical mapping

and immunocytochemical examination. Excitation patterns were visualized with a Fluo-4-AM Ca^{2+}-sensitive indicator (Molecular Probes, USA, F14201) in Tyrode's solution (Sigma-Aldrich Co., USA, T2145-10L) and recorded with an Olympus MVX10 fluorescence microscope equipped with an EM-CCD Andor iXon-3 camera (130 frames per second).

Sample generation in the model implies zero conductivity of the entire region n, which, together with the integration scheme, resulted in Neumann boundary conditions with no-flux through the border ∂n.

Experimental implementation of no-flux boundary between NRVM tissue and obstacle was achieved with SYLGARD®184 (SigmaAldrich Co., USA, Cat # 761,028) rectangular blocks adhered to culture glasses before cell seeding, Fig. 1. It was previously shown that the chosen method was sufficient to preserve a planar wavefront in the nearest vicinity of the boundary [37].
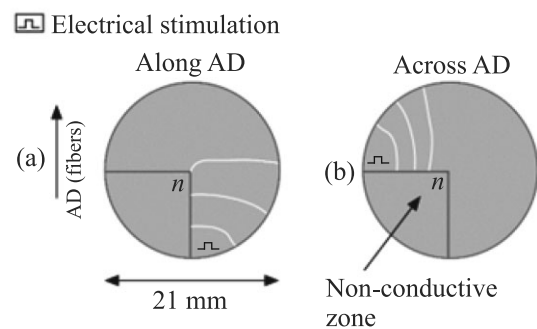

Fig. 1. Experimental scheme of symmetric no-flux boundary experimental model. Electrical stimulation of cardiomyocytes along AD (a), across AD (b). The sample is oriented in such a way that AD is directed vertically, and the non-conducting region n is located in the lower left part. A schematic step displays the location of the electrode stimulus

To characterize the structural features of anisotropic cardiac tissue, we performed an immunocytochemical examination of NRVM samples, Fig. 2a. The complex network of actin–myosin contractile filaments in cardiac tissue is arrayed into a fibrous sliding apparatus that exhibits strong anisotropy. In particular, α-actin presents long well-ordered filaments that appear as nearly parallel lines in fluorescence images. Spatial alternation of identical α-actin structures makes them amenable to fast Fourier transform (FFT) analysis [38]: approximation of the radial sums of FFT images of the Gaussian curve allowed us to assess AD as the location of the peak and AR as its half-width, Fig. 2b. The global and local directions of AD may not coincide: Fig. 2c, d shows the branching of AD in the FFT analysis of nested sections.
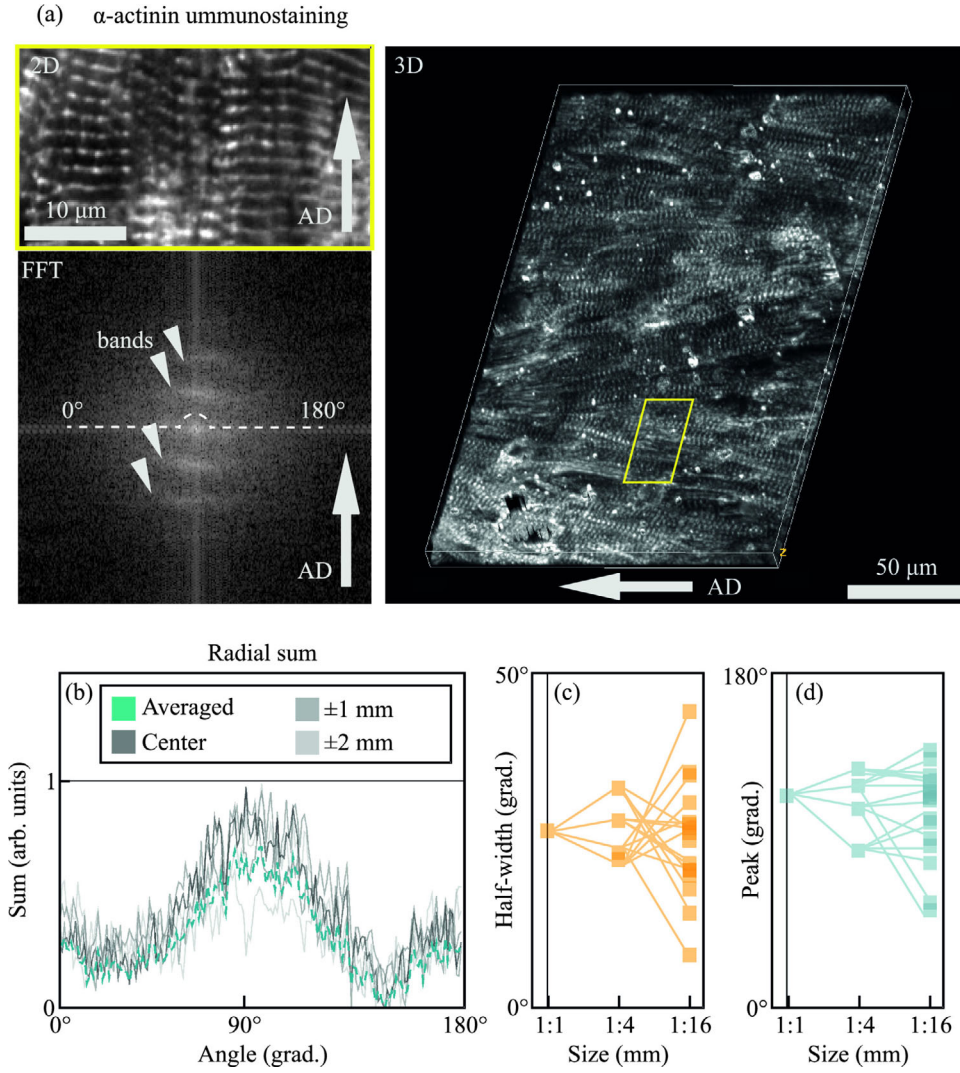
Fig. 2. (Color online) Anisotropy of a NRVM monolayer on an aligned nanofiber matrix. (a) – Confocal micrographs of a section of anisotropic tissue, FFT transformation of the pattern of transverse banding of the actinin cytoskeleton. (b) – Radial sum of the bands of the FFT transform on different confocal image slices. (c) and (d) – The radial sum Gaussian curve fitting results are presented as peak value and half-width. Using connections, the branching of the curve parameters is shown with a multiple decrease in the area under study

The similarity between our model and the tissue studied *in vitro* is formulated in two key points: the first one is the alternation of domains with different local AD, which is reproducible both *in vitro* and in CPM formalism due to the H_{protr} term [21], which specifies the local alignment of filaments; the second one is the presence of nodal points between neighboring domains: GJ and EpC (due to $H_{\text{junctions}}$ term). Separate descriptions are available for both types of heterogeneities, but here we were able to show their unification under one formalism, since the location of intercellular contacts in $H_{\text{junctions}}$ is directly related to the sites of filament protrusions obtained with H_{protr}.

A direct relationship between the biological structure and the conductive function of a sample was visualized using optical mapping of the excitation wave front at high stimulation frequencies. Visualization of disturbances of a plane wavefront propagating along the no-flux boundary is shown in Fig. 3a and b for the model (calculated dV/dt) and experiment (time derivative of the recorded Fluo-4 AM signal), respectively. The projection of multidimensional mapping data F was made in the form of space-time plots from [39], Eq. (3):

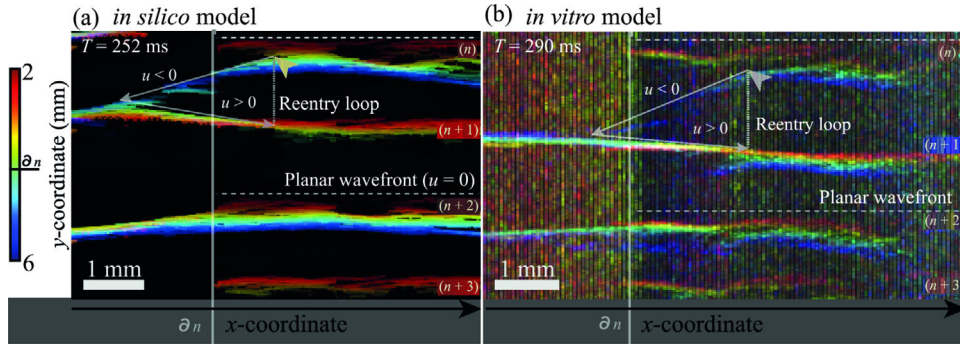$$\bar{F}(x,t) = \frac{1}{NVY} \int_0^{NVY} F(x,y,t)dy,$$

Fig. 3. (Color online) Spatio-temporal graphs of the movement of the leading wave front during the formation of reentry in a high-frequency wave train. Panels (a) and (b) present a qualitative comparison of reentry generation *in silico* ($T = 252$ ms, $D_{\text{bound}} = 5$) and *in vitro* model ($T = 290$ ms). The spatial x-coordinate is plotted along the horizontal axis, the y-coordinate is displayed through coding, and time is plotted along the vertical axis (from top to bottom). Here, u denotes the projection of the CV onto the x-axis (equal to zero for a flat wave front — approximated as a dotted horizontal line). Semi-translucent white arrows and a vertical dotted line show the closure of the reentry loop for wave (n). The ($n + 1$) wave annihilates with the resulting spiral wave

$$\bar{F}(y,t) = \frac{1}{NVX} \int_0^{NVX} F(x,y,t)dx, \qquad (3)$$

when proceeding from F to F', one of the spatial coordinates is replaced with t, and the direct display of the hidden spatial coordinate is replaced with a color-coded projection. Figure 3 shows the key features inherent in the model and the experiment: branching of the excitation front, local growth of the unidirectional block behind the acute angle of the obstacle n, closure of the reentry loop during the reverse passage of the wave through the zone of the unidirectional block.

Hence, we found that the presence of a no-flux boundary and a decrease in excitability due to high-frequency stimulation are sufficient conditions for evenly distributed deformation of the planar wavefront in anisotropic cardiac tissue. Therefore, local curvature of the boundary makes it possible to achieve "focusing" of excitation disturbances in its vicinity to construct a sufficient unidirectional block of conduction, which consistently leads to reentry formation. To achieve such structural and functional consistency between *in vitro* and *in silico* models, it was sufficient to combine the alignment of the cytoskeleton and cellular coupling formation under one common CPM formalism.

Let us consider the structural heterogeneity formulated above to be the simplest but sufficient model for reproducing functional results regarding the conditions for the formation of reentry in anisotropic cardiac tissue with inherent inhomogeneity. To check the correctness of this statement, we tried to obtain a solution to a simple problem concerning changes in conduction anisotropy: how does the set of T_{crit} differ when stimulating a sample along AD and across it?

As a null hypothesis, we evaluated the estimated distribution of T_{crit} in a homogeneous model using the eikonal equation [40, 41]. This relationship in adaptation to autowaves connects the CV value C with the local curvature of the active medium. In a homogeneous model, tissue anisotropy could be formulated as $D_x > D_y$ for all the elements of the excitable medium. The symmetry of the sample deduces the radius of curvature of the non-conducting zone from the equation and simplifies the expression to $\Delta C \sim D$ in the vicinity of the obstacle, where D is the local conductivity after passing through a rectangular angle; that is, perpendicular to the initial direction of the wavetrain. In this case, stimulation across AD gives a larger change in CV ($D_x > D_y$) and, therefore, a larger wavefront deformation in the vicinity of the obstacle's tip. Finally, if MCR is assumed to be independent of the stimulation site, then for all $T > MCR$, ΔC for stimulation across AD should be greater than ΔC for stimulation along AD as well as unidirectional block probability. Therefore, the analysis of a homogeneous model gave rise to the following null hypothesis: high-frequency stimulation of the sample across AD results in a wider set of T_{crit} values due to a higher upper bound on the set (lower bound limited by MCR in both cases).

We used two heterogeneous models of cardiac tissue described above to test this hypothesis. In the computational model, we moved along integer values of electrode stimulation period T (ms) and compared the behavior of the excitation waves when stimulating the sample along the AD and across it (Fig. 4).

Figure 4a shows the formation of a spiral wave due to the dynamic growth of a unidirectional block that
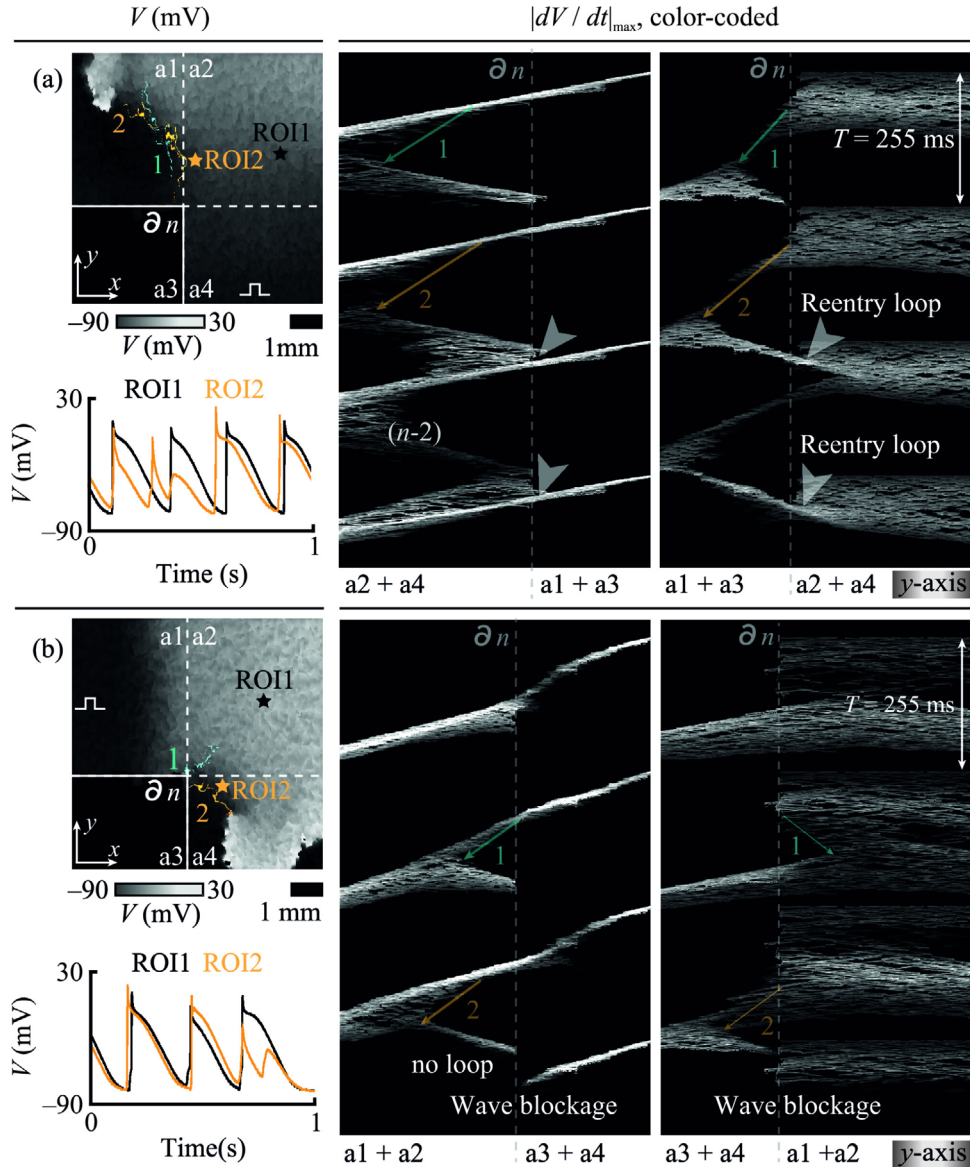
Fig. 4. (Color online) Spatio-temporal plots of the movement of the leading wavefront during stimulation along (a) and across (b) the AD. Both panels display a computer model of the sample at the same stimulation period $T = 255$ ms and $D_{\text{bound}} = 15$. The orange and cyan colors show a unidirectional block forming in a wave train: number 1 indicates the block preceding 2, the maximum detected block in the simulation. In case (a), the combination of the stimulation period T and the size of the unidirectional block is sufficient to close the reentry loop. In case (b), the closure of the reentry loop does not occur, which leads to a block of the subsequent wave. Graphs V (time) display local rhythm disturbances in the indicated ROIs near the site of unidirectional block formation

occurred when the sample was stimulated along the AD. The T value at which the closure of the reentry loop is achievable can be attributed to the T_{crit} subset. Figure 4b shows the impossibility of closing the reentry loop at the same period T when the sample was stimulated across the AD. Space-time plots show that the combination of an appropriate time interval between waves and a steady increase in a unidirectional block during the passage of subsequent waves are nec-

essary for the complete closure of the loop, as shown in Fig. 4a.

A comparison of computer and experimental modeling is presented below, Fig. 5a, b and c, respectively. With computational model, we examined all integer values of electrode stimulation period T from 240 to 275 ms. The D_{bound} value was also used as a variable parameter due to the lack of accurate experimental measurements for a monolayer of NRVMs on nanofibers.
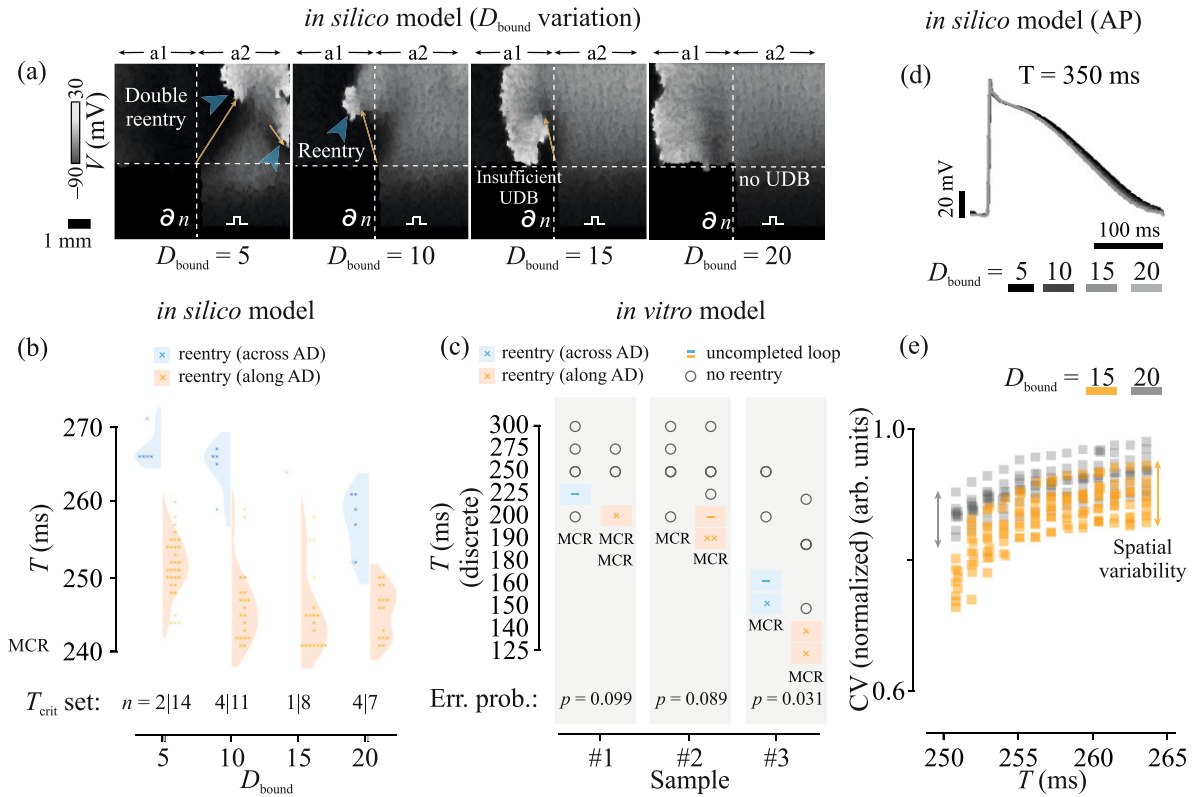
Fig. 5. (Color online) (a) – Spatial distribution of V at different values of D_{bound} (*in silico* model). All images reflect the location of the excitation wave at the same time point, 1.814 s from the start of the stimulation protocol ($T = 250$ ms). (b) – Dotted and violin plots showing the distribution of T_{crit} at different values of D_{bound}. (c) – Estimation of T_{crit} distribution in experiments on NRVM monolayers. (d) – Variability of the action potential when passing through tissue with different D_{bound}. (e) – CV restitution curve relative to the stimulation period T: the graph compares the spatial variability of CV and its dependence on D_{bound}

This set of parameters allowed us to reproduce all combinatorially possible options: stimulation of the sample on both sides does not lead to reentry formation, reentry occurs in both cases (T_{crit} for both cases), and reentry occurs at T_{crit} only in one stimulation variant (out of two). The experimental model showed qualitative consistency with simulation results in terms of T_{crit} distribution, Fig. 5c. All the *in vitro* experiments were limited to five stimulation protocols per stimulation site (along and across AD for three samples) to minimize damage to the samples during high-frequency stimulation.

If a heterogeneous computer model clearly rejected the null "homogeneous" hypothesis, then finite statistics in the experiment left behind some probability of the null hypothesis being partially realized. In particular, the increased width of the T_{crit} corridor during stimulation across the AD could be considered as a necessary but not sufficient condition for the null hypothesis to be fulfilled. We calculated all continuous integer variations of T_{crit} that fit into the experimental data grid: the captions in Fig. 5c show at what proportion

of possible combinations (p) at least the necessary part of the null hypothesis could be realized. On the other hand, the resulting data grid per se excludes the fulfillment of the null hypothesis, thereby being consistent with computer modeling and forming a hypothesis: high-frequency stimulation of the sample along AD (instead of across AD) results in a wider set of T_{crit} values, shifted towards higher stimulation frequencies and MCR.

Finally, we examined the modulation of intercellular coupling parameters, Fig. 5d–f. It was found that changes in wave dynamics with varying D_{bound} (EpC) had a specific pattern: changes in arrhythmogenicity (T_{crit}) were significant, while changes in CV and RP varied within the range of values, Fig. 5d–f. This phenomenon indicated the complex nature of the relationship between the microscopic parameters of the cells and the behavior of the macroscopic system (anisotropic tissue) that allows the occurrence and maintenance of reentry: modulation of D_{bound} entered into a selective change in the properties of the system, which would not

be possible in a homogeneous model, where CV directly depends on D, or with modulation of GJ [8, 10].

The "structure/function" paradigm is one of the central cores in modern biology and physiology [42], becoming the touchpoint between physical and biological research in problems of G protein-coupled receptors, protein folding [43] and other aspects of structural biology. Cardiac contraction is accompanied by the coordination of a large number of processes occurring at different levels of organization with inherent structural complexity. Thus, we attempted to extend the "structure/function" paradigm to a biological system at a higher level of organization by uniting subcellular structures and self-organized multicellular clusters under a common CPM formalism. As a result, we derived a theoretical formulation of CV anisotropy and validated it through *in vitro* and *in silico* functional experiments as an effective tool for predicting reentry.

The following considerations can be provided to discuss the specific symmetry breaking mechanism. Propagation of excitation waves through the sample causes the following chain of events, Fig. 4a. First, a wavetrain begins to propagate through the tissue with uniformly distributed inhomogeneities (however, not randomly, since the geometry of all cells obeys a steady minimum of the Hamiltonian of the system). Further, the geometric obstacle creates a local sink-source mismatch at the boundary a1/a2, thereby locally "focusing" functional disturbances in the form of a unidirectional block. From this moment on, "structural" heterogeneities and "functional" ones cease to coincide. The further evolution of the system implies two scenarios: either the wave overcomes the unidirectional block, thereby restoring the coherence between structural and functional inhomogeneities, or the unidirectional block continues to grow. Obviously, if the block size exceeds the characteristic size of the reentry core, then the front's overcoming of the a1/a2 boundary will lead to reentry formation (incoherence of functional and structural heterogeneities would be locally preserved in the reentrant core) rather than to coherence restoration. Sustained growth of a unidirectional block was observed more often with stimulation along AD (Fig. 5a–c): this may be explained by the fact that the a1/a2 boundary largely consists of well-aligned lateral sides of cells (Fig. 2 in [44]), conduction between which is mainly provided by EpC. In the case of stimulation across AD, growth of a unidirectional block is less stable (a2/a4), since the transverse sides of the cells are less ordered and also have greater conductivity (greater GJ density). This line of reasoning can be extrapolated to human atrial tissue due to the similar nature of cell alignment [45, 46].

The point where theoretical calculations and biophysical experiment in this work intersect is the determination of the set of T_{crit} values in which reentry generation occurred. From an experimental point of view, this approach is widely used, since in practice, the frequency corridor can be either infinitely wide [47] in special cases (I_{Na} inhibition) or wide enough for registration in the general case (without channel blockers) [48]. The characteristic size of the corridor could be estimated as 10 % of the AP duration [46], i.e. 20–40 ms for the vast majority of experimental models. On the contrary, calculations using homogeneous theoretical models predict a frequency corridor that seems to be too narrow for practical registration (about 5–10 ms), which casts doubt on the importance of the "geometrical" mechanism of the reentry onset [16]. Judging by our results, adding intercellular heterogeneities to the model allows us to achieve a realistic width of the T_{crit} corridor (about 10 % of AP), which in turn restores the agreement between theory and experiment and rehabilitates the significance of the "geometrical" mechanism in the overall picture of arrhythmogenesis. Apparently, we managed to break the one-to-one correspondence between the values of D and CV: if it is traditionally believed that CV and RP can be used as reliable parameters for fitting a model to an experiment, then it is possible that they should be supplemented with an estimate of T_{crit} for adjusting EpC and GJ conduction.

Computational studying of EpC has a direct application to assessing pro- and anti-arrhythmogenic drug effects. To efficiently test substances, one needs to understand how cell uncoupling in general [48] (and a decrease in intracellular conductance without affecting the GJ in particular [31]) affects the conductive properties of the tissue. Such effects cannot be predicted by standard patch-clamp studies, but in their absence, the results of tissue experiments may be inexplicable like it was in [35]. Our theoretical approach will be useful for studying cases where non-selective modulation of ion channels can synergize with changes in EpC: presumably, when an active substance is introduced into a cell membrane and could change both the properties of transmembrane proteins and the conditions for the formation of EpC between the membranes of neighboring cells [35, 48].

To sum up, joint theoretical and experimental analysis of the relationship between the cardiac tissue structure and its function revealed two aspects. The first one consisted in limitation of the applicability of the homogeneous formulation of conduction anisotropy when studying primary reentry, since the nature of intercellular heterogeneities plays a crucial role in the sustainable growth of a unidirectional block. The second one

showed up in the distinct role of EpC and GJ in stabilizing the high-frequency wavetrain, which modulates tissue arrhythmogenicity bypassing the well-known factors such as modulation of ionic currents.

Conflicts of interest. The authors declare no conflict of interest. The funders had no role in the design of the study; in the collection, analyses, or interpretation of data; in the writing of the manuscript; or in the decision to publish the results.

Ethics approval and consent to participate. All the experimental studies conformed to the Guide for the Care and Use of Laboratory Animals published by the United States National Institutes of Health (Publication # 85-23, revised 1996) and approved by the Moscow Institute of Physics and Technology Life Science Center Provisional Animal Care and Research Procedures Committee, Protocol # A2-2012-09-02.

1. B. P. Belousov, *Collection of Short Papers on Radiation Medicine for 1958*, Meditsina Publishers, Moscow (1959), p. 145, in Russian.

2. A. N. Zaikin and A. M. Zhabotinsky, Nature **225**(5232), 535 (1970).

3. G. T. Gerisch, Wilhelm Roux'Archiv fur Entwicklungsmechanik der Organismen **156**(2), 127 (1965).

4. C. J. Weijer, Current opinion in Genetics & Development **14**(4), 392 (2004).

5. N. A. Gorelova and J. Bures, Journal of Neurobiology **14**(5), 353 (1983).

6. D. P. Zipes and J. Jalife, *Cardiac Electrophysiology: From Cell to Bedside E-Book: Expert Consult*, Elsevier Health Sciences, Philadelphia (2009).

7. R. Majumder, T. De Coster, N. Kudryashova, A. O. Verkerk, I. V. Kazbanov, B. Ördög, N. Harlaar, R. Wilders, A. A. F. de Vries, D. L. Ypey, A. V. Panfilov, and D. Pijnappels, Elife **9**, e55921 (2020).

8. K. Maciunas, M. Snipas, T. Kraujalis, L. Kraujaliene, and A. V. Panfilov, Sci. Rep. **13**(1), 14863 (2023).

9. W. C. Cole, J. B. Picone, and N. Sperelakis, Biophys. J. **53**(5), 809 (1988).

10. S. H. Weinberg, Chaos: An Interdisciplinary Journal of Nonlinear Science **27**(9), 093908 (2017).

11. A. Panfilov and P. Hogeweg, Phys. Lett. A **176**(5), 295 (1993).

12. M. Bär and M. Eiswirth, Phys. Rev. E **48**(3), R1635 (1993).

13. A. Karma, Phys. Rev. Lett. **71**(7), 1103 (1993).

14. S. Alonso, R. Kapral, and M. Bär, Phys. Rev. Lett. **102**(23), 238302 (2009).

15. D. N. Hajian, F. Parastesh, S. Jafari, M. Perc, and E. Klemenčič, Chaos, Solitons & Fractals **179**, 114413 (2024).

16. A. V. Panfilov, Phys. Rev. E **59**(6), R6251 (1999).

17. S. Hussaini, S. L. Lädke, J. Schröder-Schetelig, V. Venkatesan, R. A. Quiñnonez Uribe, C. Richter, R. Majumder, and S. Luther, PLOS Comput. Biol. **19**(12), e1011660 (2023).

18. K. Agladze, R. R. Aliev, T. Yamaguchi, and K. Yoshikawa, J. Phys. Chem. **100**(33), 13895 (1996).

19. A. G. Kléber and Y. Rudy, Physiol. Rev. **84**(2), 431 (2004).

20. S. Kadota, M. W. Kay, N. Magome, and K. Agladze, JETP Lett. **94**, 824 (2012).

21. N. Kudryashova, A. Nizamieva, V. Tsvelaya, A. V. Panfilov, and K. I. Agladze, PLOS Comput. Biol. **15**(3), e1006597 (2019).

22. J. Sánchez, J. F. Gomez, L. Martinez-Mateu, L. Romero, J. Saiz, and B. Trenor, Frontiers in Physiology **10**, 847 (2019).

23. R. Majumder, M. C. Engels, A. A. F. de Vries, A. V. Panfilov, and D. A. Pijnappels, Sci. Rep. **6**(1), 24334 (2016).

24. I. V. Kazbanov, K. H. W. J. ten Tusscher, and A. V. Panfilov, Sci. Rep. **6**(1), 20835 (2016).

25. N. Kudryashova, V. Tsvelaya, K. Agladze, and A. Panfilov, Sci. Rep. **7**(1), 7887 (2017).

26. G. Francois and J. A. Glazier, Phys. Rev. Lett. **69**(13), 2013 (1992).

27. J. A. Glazier and G. Francois, Phys. Rev. E **47**(3), 2128 (1993).

28. A. Gamba, D. Ambrosi, A. Coniglio, A. de Candia, S. Di Talia, E. Giraudo, G. Serini, L. Preziosi, and F. Bussolino, Phys. Rev. Lett. **90**(11), 118101 (2003).

29. A. Kalinin, V. Naumov, S. Kovalenko, A. Berezhnoy, M. Slotvitsky, S. Scherbina, A. Aitova, V. Syrovnev, M. Popov, A. Kalemberg, S. Frolova, K. Agladze, and V. Tsvelaya, J. Appl. Phys. **134**(5), 054702 (2023).

30. K. Agladze, J. P. Keener, S. C. Müller, and A. Panfilov, Science **264**(5166), 1746 (1994).

31. A. D. Podgurskaya, M. M. Slotvitsky, V. A. Tsvelaya, S. R. Frolova, S. G. Romanova, V. A. Balashov, and K. I. Agladze, Sci. Rep. **11**(1), 2336 (2021).

32. R. Stanley and H. Larsen, IEEE Transactions on Biomedical Engineering **4**, 389 (1978).

33. M. Clerx, P. Collins, E. De Lange, and P. G. A. Volders, Prog. Biophys. Mol. Biol. **120**(1–3), 100 (2016).

34. M. Courtemanche, R. J. Ramirez, and S. Nattel, Am. J. Physiol. Heart Circ. Physiol. **275**(1), H301 (1998).

35. A. A. Nizamieva, I. Y. Kalita, M. M. Slotvitsky, A. K. Berezhnoy, N. S. Shubina, S. R. Frolova, V. A. Tsvelaya, and K. I. Agladze, Chaos: An Interdisciplinary Journal of Nonlinear Science **33**(2), 023112 (2023).

36. A. Aitova, S. Scherbina, A. Berezhnoy et al. (Collaboration), Int. J. Mol. Sci. **24**(12), 10406 (2023).

37. V. N. Kachalov, V. A. Tsvelaya, N. N. Kudryashova, and K. I. Agladze, JETP Lett. **106**, 608 (2017).

38. Y. Orlova, N. Magome, L. Liu, Y. Chen, and K. Agladze, Biomaterials **32**(24), 5615 (2011).

39. J. M. Davidenko, A. V. Pertsov, R. Salomonsz, W. Baxter, and J. Jalife, Nature **355**(6358), 349 (1992).

40. M. Hörning, A. Isomura, Z. Jia, E. Entcheva, and K. Yoshikawa, Phys. Rev. E **81**(5), 056202 (2010).

41. A. R. Bruss, J. Math. Phys. **23**(5), 890 (1982).

42. P. Liu, E. M. Leung, M. A. Badshah, C. S. Moore, and A. A. Gorodetsky, APL Bioeng. **7**(4), 046111 (2023).

43. P. Chandarana, N. N. Hegade, I. Montalban, E. Solano, and X. Chen, Phys. Rev. Appl. **20**(1), 014024 (2023).

44. I. S. Erofeev and K. I. Agladze, JETP Lett. **100**, 351 (2014).

45. P. Camelliti, Th. K. Borg, and P. Kohl, Cardiovasc. Res. **65**(1), 40 (2005).

46. M. M. Peters, J. K. Brister, E. M. Tang, F. W. Zhang, V. M. Lucian, P. D. Trackey, Z. Bone, J. F. Zimmerman, Q. Jin, F. J. Burpo, and K. Parker, APL Bioeng. **7**(4), 046114 (2023).

47. C. Cabo, A. M. Pertsov, J. M. Davidenko, W. T. Baxter, R. A. Gray, and J. Jalife, Biophys. J. **70**(3), 1105 (1996).

48. A. D. Podgurskaya, V. A. Tsvelaya, S. R. Frolova, I. Y. Kalita, N. N. Kudryashova, and K. I. Agladze, Toxicol. Vitro **51**, 136 (2018).